arXiv:1612.01451v1 [astro-ph.EP] 5 Dec 2016

A simple model for the location of Saturn's F ring

Luis Benet[a,*], Àngel Jorba[b]

[a] *Instituto de Ciencias Físicas, Universidad Nacional Autónoma de México (UNAM)*
Apdo. Postal 48–3, 62251 Cuernavaca, Mexico
[b] *Departament de Matemàtica Aplicada i Anàlisi, Universitat de Barcelona*
Gran Via 585, 08007 Barcelona, Spain

Abstract

In this paper, we introduce a simplified model to understand the location of Saturn's F ring. The model is a planar restricted five-body problem defined by the gravitational field of Saturn, including its second zonal harmonic J_2, the shepherd moons Prometheus and Pandora, and Titan. We compute accurate long-time numerical integrations of (about 2.5 million) non-interacting test-particles initially located in the region between the orbits of Prometheus and Pandora, and address whether they escape or remain trapped in this region. We obtain a wide region of initial conditions of the test particles that remain confined. We consider a dynamical stability indicator for the test particles' motion defined by computing the ratio of the standard deviation over the average value of relevant dynamical quantities, in particular, for the mean-motion and the semi-major axis. This indicator separates clearly a subset of trapped initial conditions that appear as very localized stripes in the initial semi-major axis and eccentricity space for the most stable orbits. Retaining only these test particles, we obtain a narrow eccentric ring which displays sharp edges and collective alignment. The semi-major axis of the accumulation stripes of the stable ring-particles can be associated with resonances, mostly involving Prometheus' outer Lindblad and co-rotation resonances, but not exclusively. Pandora's inner Lindblad and co-rotation resonances as well as low-order three-body resonances typically coincide with gaps, i.e., regions of instabilities. Comparison of our results with the nominal data for the F ring shows some correspondence.

*Corresponding author
Email addresses: benet@fis.unam.mx (Luis Benet), angel@maia.ub.es (Àngel Jorba)

Keywords: Saturn, rings, Planetary rings, Resonances, rings

1. Introduction

Saturn's F ring is a fascinating narrow ring with a rich time-varying structure, which has puzzled dynamical astronomers since its discovery by the Pioneer 11 team in 1979 (Gehrels et al., 1980). It is located outside Saturn's A ring, close but beyond Roche's limit for ice, and is believed to be the result of the ongoing action of competing accretion and disruptive processes (Barbara and Esposito, 2002). The F ring is narrow, non-circular and inclined, has azimuthal dependent properties which may change on time, and displays certain localized radial structures (Porco et al., 2005). It consists of a dense core ($1-40$ km) embedded in a broader belt of dust (~ 700 km), with additional separated dusty components named strands, the most prominent form one-arm kinematic spirals on either side of the core (Charnoz et al., 2005). It also contains an underlying belt of forming moonlets (Cuzzi and Burns, 1988) that produce the observed "fan" structures (Murray et al., 2008; Beurle et al., 2010), and whose collisions with the core manifest as jets (Murray et al., 2008). For recent reviews see Colwell et al. (2009, sect. 13.5) and Charnoz et al. (2009).

The F ring is perturbed by the shepherd moons Prometheus and Pandora, that orbit on either side of the ring. The discovery of these moons (Smith et al., 1981, 1982) was initially interpreted as the success of the confinement produced by the shepherding mechanism, proposed by Goldreich and Tremaine (1979). Yet, the torques from the shepherd moons do not balance out at the location of the ring (Showalter and Burns, 1982). Moreover, the shepherd moons orbit around Saturn on seemingly chaotic orbits (Poulet and Sicardy, 2001; French et al., 2003; Goldreich and Rappaport, 2003a,b). While it is clear that Prometheus and Pandora play an important role on the dynamics and structure of the ring (Showalter and Burns, 1982; Winter et al., 2007), it is not clear what is the actual mechanism that keeps the ring confined at its location (Esposito, 2006).

Some of the structural phenomena described above have been analyzed previously through numerical simulations. For instance, using independent test particle models with periodic boundary conditions along the azimuthal direction, Giuliatti Winter et al. (2000) integrated the equations of motions

of the circular restricted three-body problem of Saturn and Prometheus up to a few tens of revolutions. They showed that, after a close approach with this moon, ring particles initially located at the strands of the F ring were scattered inwards and outwards, forming gaps and waves; these were later confirmed by Cassini, and were named channels (Porco et al., 2005). These calculations were taken further (Murray et al., 2005), concluding that streamers and channels are part of the same phenomenon and can be understood in terms of the gravitational interaction with this moon and its eccentric motion. Other calculations considered the effect of Pandora during 160 yr, and concluded that the motion of embedded moonlets in the the ring is likely chaotic, removing it from the F ring region (Giuliatti Winter et al., 2006). Charnoz et al. (2005) discovered a kinematic spiral strand and interpreted it, based on numerical simulations spanning 2000 orbital periods, as the effect of interactions with small satellites in the F ring region. More complex integrations, including 14 massive Saturn moons and spanning tens of thousands of Prometheus periods, were conducted by Cuzzi et al. (2014), and led them to the conclusion that certain regions of stability arise because the perturbations induced by an encounter with Prometheus are counter-balanced by subsequent encounters with the same shepherd.

While these investigations have clarified the influence of the shepherd moons in the variations on the structure of the F ring, the question of its confinement remains unanswered. The question can be restated in terms of the location of the ring. The fact that the shepherd moons move on chaotic trajectories makes this problem more interesting since, strictly speaking, it breaks the periodicity of the perturbations. With regards to this, it is worth quoting Tiscareno (2013), who points out that, despite the time-varying clumpy and kinky structure, the F ring core "maintains over decadal timescales the shape of a freely precessing eccentric inclined ellipse; the orbital solution formulated to account for Voyager and other pre-Cassini data (Bosh et al., 2002) has, somewhat surprisingly, remained a good predictor of the core's position through the Cassini mission".

In this paper we address the question of the confinement and location of Saturn's F ring within an independent (non-interacting) test particle model. We consider a simplified planar restricted five-body model and follow the dynamics of a large number of test particles (~ 2.5 millions) up to 6×10^6 orbital revolutions of Prometheus, slightly more than 10000 years. The model includes the gravitational field of Saturn with its second gravitational harmonic J_2, Prometheus, Pandora and Titan; preliminary results appear in (Benet

and Jorba, 2013). We find a broad set of test-particle initial conditions that remain trapped within the region between Prometheus and Pandora. Within this set, there are initial conditions that remain well-localized and correspond to the more stable ones with respect to their radial excursions. A projection onto the $X-Y$ space of a snapshot of this stable subset yields a narrow and eccentric ring with collective alignment, whose location properties and width can be compared with the observations.

The model we consider is simple in the sense that it does not include contributions which are important for a detailed realistic description, such as the J_4 gravitational harmonic or the gravitational interaction of other Saturn moons. The assumption of non-interacting test particles is equivalent to neglecting any ring particle collisions and self-gravity. While the assumptions are rather strong, in particular for the time-span of our integrations, our view is that the physics of the existence of the F ring, or other phenomena, is not related to matching very specific parameters, but because certain necessary conditions are fulfilled. In the present case, the important property is the existence of phase-space regions where the radial diffusion is strongly suppressed.

The paper is organized as follows: In section 2 we describe of our general approach and introduce the simple model that we study. Section 3 describes the numerical results obtained, where we focus first on the test particles that remain trapped up to a maximum time, and then classify them dynamically according to their stability. The stability analysis is based on a dimensionless dynamical indicator related to the radial excursions. *Filtering* the orbits that do not satisfy a stability condition yields a narrow, eccentric, sharp-edged ring, whose semi-major axis and width are then compared with the observations. We relate the accumulation in the semi-major axis of the ring particles, and the gaps between them, to orbital resonances, which involve mainly Prometheus outer Lindblad and co-rotation resonances, but not exclusively. Finally, in section 4 we summarize our approach and results.

2. A simplified model for Saturn's F ring: the scattering approach

A complete description of the dynamics of Saturn's F ring must contain the gravitational interactions of Saturn including its flattening, the influence of all Saturn's moons including in particular the shepherd moons, Prometheus and Pandora, and the interactions among the ring particles themselves. The latter involves non-trivial processes associated with physical

collisions among the particles of the ring, such as accretion and fragmentation processes (Attree et al., 2012, 2014), which are particularly relevant because the F ring is located near the edge of the Roche zone (Canup and Esposito, 1995). Needless to say, the understanding of such a system is difficult. Here, we shall study a simpler model with the hope that it may clarify some aspects of the confinement of Saturn's F ring.

Our approach is based on the observation that some test particles eventually "escape" from the proximity of the ring, while others remain trapped; the latter are those we observe. This is the essence of the scattering approach to narrow rings (Benet and Seligman, 2000; Merlo and Benet, 2007). Consider the planar motion for the ring particles, which are assumed independent massless test particles, i.e., mutual collisions are neglected. For a short-range potential moving on a circular orbit around the central planet, one can prove that there exist stable periodic orbits in phase space (Benet and Seligman, 2000). The linear stability of such orbits and KAM theory (de la Llave, 2001) in a two degrees of freedom system suffice to show that initial conditions which are close enough to the stable periodic orbits are dynamically trapped. Initial conditions beyond certain distance, essentially given by the invariant manifolds of a central unstable periodic orbit in the vicinity, will escape along scattering trajectories. The whole region of trapped motion in phase space, which includes different values of the conserved quantity (Jacobi constant), is of central interest. In particular, the projection of this region onto the $X - Y$ space forms a narrow ring; its narrowness follows from the actual (small) region of trapped orbits in phase space. The ring may be eccentric, since it mimics the projection of the central stable periodic orbit in the $X - Y$ space, which in general is non-circular. Non-circular motion of the short-range potential implies an extended phase-space, due to the explicit time-dependence of the Hamiltonian, which may produce a richer structure, e.g., multiple components and arcs (Benet and Merlo, 2008, 2009). For small enough perturbations, the stable organizing centers of the dynamics are preserved, which in turn preserves the region of trapped motion in phase space that sustains the ring. The scattering approach is, in that sense, robust (Benet and Seligman, 2000).

The starting point of our model (Benet and Jorba, 2013) is to consider the motion of an ensemble of non-interacting massless test particles, defined by the initial conditions which are in the proximity of the location of the F ring. Their time evolution shall determine whether a test particle remains (dynamically) trapped and hence belongs to the ring, or if it simply escapes away.

Certainly, this starting point entails a number of non-realistic assumptions, which lead to some simplifications. Considering non-interacting test particles allows us to treat each particle independently, i.e., we may consider a one-particle Hamiltonian; different initial conditions represent different particles. In doing this, we neglect any effects due to mutual collisions or related to their actual shape and size. These properties are important for a detailed understanding of the fine structure and life-time of the ring (Poulet et al., 2000; Murray et al., 2008; Charnoz et al., 2009). We shall also disregard the influence of the whole ring in the motion of any of the major bodies or of the particles of the ring; this is tantamount of having massless test particles. We assume for simplicity that the motion of all bodies takes place in the equatorial plane of Saturn. These assumptions allow us to consider a planar restricted $(N+1)$-body problem, where a test particle is influenced by the motion of N massive bodies.

The model is naturally divided into two parts. First, the motion of the N-interacting massive bodies is given by the many-body Hamiltonian

$$\mathcal{H}_N = \sum_{i=0}^{N-1} \frac{1}{2m_i}(P_{x_i}^2 + P_{y_i}^2) - \sum_{i=1}^{N-1} \frac{\mathcal{G}m_0 m_i}{R_{i,0}}\Big(1 + \frac{J_2}{2}\frac{R_S^2}{R_{i,0}^2}\Big) - \sum_{1\le i<j}^{N-1} \frac{\mathcal{G}m_i m_j}{R_{i,j}}. \quad (1)$$

Here, $\vec{R}_i$ is the position vector of the i-th body with respect to the origin of an inertial frame, $\vec{P}_i$ denotes the canonically conjugated momentum and m_i its mass. We denote by $R_{i,j} = |\vec{R}_i - \vec{R}_j|$ the relative distance between two bodies and use the convention that $i = 0$ represents Saturn, and its moons are ordered increasingly with respect to their nominal semi-major axis.

In our calculations we use Saturn's mass $m_0 = 5.68319 \times 10^{26}\,\mathrm{kg}$ as the unit of mass (Jacobson et al., 2006), Saturn's equatorial radius $R_S = 60268.0\,\mathrm{km}$ as the unit of distance (Seidelmann et al., 2007)[1], and Prometheus period $T_{\mathrm{Prom}} = 0.612986\,\mathrm{days}$ (Seidelmann et al., 2007) as 2π units of time

[1]Note that R_S corresponds to the 1 bar surface equatorial radius of Saturn (Seidelmann et al., 2007), and was naively retrieved from the JPL-Horizons Physical Data and Dynamical Constants table for the planets (`http://ssd.jpl.nasa.gov/?planet_phys_par`). This value was used to scale out the semi-major axis (obtained from the J_2 first order corrections and the observed mean motion) to set-up our numerical calculations. This value is not the standard one used in the planetary rings literature; the latter is $R_S' = 60330\,\mathrm{km}$ and is also the nominal value used to compute the zonal harmonics of Saturn (Nicholson and Porco, 1988; Jacobson et al., 2006), in particular, the value for J_2 that we use. Below, whenever we convert a distance back to km for comparisons with the actual data, we use

(i.e., Prometheus' mean motion is unity). In these units, the numeric value of the gravitational constant is $\mathcal{G} \cong 12.311....$ In Eq. (1) we have included the first zonal gravitational coefficient of Saturn, $J_2 = 16290.71 \times 10^{-6}$ (Jacobson et al., 2006), since we are interested in somewhat long-time integrations. Higher-order zonal harmonics have been ignored, since they do not create new resonances and slow down significantly the numerical calculations; yet, these corrections are important for realistic models (Renner and Sicardy, 2006; El Moutamid et al., 2014). As a side remark, we mention that including the flattening of Saturn actually allows to apply KAM theory in the context of the scattering approach, since the shift in the frequencies lifts up the degeneracy of the dominating two-body Kepler problem.

The second part of the model is related to the motion of the test particles. The Hamiltonian for the massless test-particles reads

$$\mathcal{H}_{\rm rp}(t) = \frac{1}{2}(p_x^2 + p_y^2) - \frac{\mathcal{G}m_0}{r_0(t)}\Big(1 + \frac{J_2}{2}\frac{R_S^2}{r_0^2(t)}\Big) - \sum_{i=1}^{N-1}\frac{\mathcal{G}m_i}{r_i(t)}, \qquad (2)$$

where $r_i(t) = |\vec{r} - \vec{R}_i(t)|$ is the relative distance of the test particle and the i-th body, $\vec{r}$ denotes the position vector of the ring particle and $\vec{p}$ its momentum. Because of the explicit appearance of time in Eq. (2), the energy of a test particle is not conserved.

What massive bodies shall we include in a simplified model for the F ring? Clearly, we must include the shepherd moons Prometheus and Pandora, which are known to influence the dynamics of the ring, though they do not confine it completely (see Esposito, 2006). Since the masses of the shepherd moons are exceedingly small, their influence on the test particles is essentially local: Test particles in the region between the shepherds, experiencing the gravitational field of Saturn and the shepherds, move along precessing Kepler ellipses which are locally perturbed by the shepherds. The time scale for the test particles to escape is extremely large, if finite at all. We shall include the interaction of another Saturn's moon with the hope that it helps promoting radial excursions and thus escapes; the model is then a planar restricted $(4+1)$-body problem.

There is no obvious choice for the third moon in the model; see Table 1 for a comparison of the orbital parameters of the main candidates and the

for the conversion factor $R_S' = 60330\,\mathrm{km}$ used in the literature. The reader is warned about this subtle inconsistency.

F ring. Two obvious candidates are Titan and Mimas: Titan is the most massive moon of Saturn's satellite system, $M_{\rm Titan} \approx 2.3669 \times 10^{-4} M_S$, and moves on a slightly eccentric orbit, but it is located rather far away from the ring, $a_{\rm Titan} = 1221.47 \times 10^3$ km. In turn, Mimas is the major moon of Saturn closest to the F ring. Moreover, Mimas could play an important role, since Pandora is close to a $3:2$ co-rotation eccentric resonance with Mimas. Its orbital eccentricity is smaller but comparable to that of Titan. Yet, its mass is rather small, $M_{\rm Mimas} \approx 6.6 \times 10^{-8}\, M_S$. The force exerted by Titan on a test particle at the nominal semi-major axis of the F ring, $a_{\rm Fring} = 140221.6\,{\rm km} \approx 2.324243...\, R'_S$, (Bosh et al., 2002), is about 4 times larger than the force exerted by Mimas, when Titan is at the location furthest from the particle and Mimas is at the closest one. In addition, Cuzzi et al. (2014, see Appendix B) remark that numerical integrations without Titan shift the location and order of the Prometheus' outer Lindblad resonances, which play an important role, as we shall also show. To keep the model simpler as possible, we shall consider only the influence of Titan on a precessing Kepler elliptic orbit. We are thus assuming that Titan's mass and eccentric motion helps to create instabilities in the region of the ring that promote escapes from that region, though allowing for the existence of regions of stable motion. Numerical calculations with and without Titan show that Titan indeed promotes radial excursions, though the actual effect is weak; see Appendix A. Due to the small mass ratio between Titan and Saturn and the shepherds and Titan, we shall simplify the numerics by computing the precessing motion of Titan due to the gravitational attraction of Saturn and its J_2 coefficient only, and for the shepherds we include the additional perturbations by Titan. We also consider that Saturn remains at the origin.

We are interested in the existence of regions of trapped motion for test particles between the orbits of the shepherd moons. The conditions for escape are defined as follows: A test particle escapes if it leaves the region defined by the orbits of the shepherds, i.e., if it is not located within the region defined by the innermost radial position of Prometheus and the outermost of Pandora; these distances are defined from their nominal locations; c.f. Table 1. In addition, we consider that a test particle collides with a shepherd moon if it is located within Hill's radius of the moon, that is, $r_i < R_{H_i} = a_i (m_i/(3m_0))^{1/3}$ (with $i = 1, 2$ for Prometheus and Pandora respectively). In this case, the test particle shall also be treated as an *escaping* particle, since such an event corresponds to a physical collision with one of the shepherds (Ohtsuki, 1993). In either case, the integration of the orbit is terminated and the test particle

Table 1: Saturn's moons and F ring data, taken from the JPL Horizons's ephemerids web interface. The semi-major axis and eccentricity of the F ring, which we shall consider as the nominal values, are taken from Bosh et al. (2002, fit 2 of Table III).

Object	a (10^3 km)	e	m (10^{19} kg)
Prometheus	139.35	0.0024	0.014
F Ring	140.2216	0.0025	?
Pandora	141.70	0.0042	0.013
Mimas	185.54	0.0196	3.75
Encedalus	238.04	0.0047	10.805
Tethys	294.67	0.0001	61.76
Dione	377.42	0.0022	109.57
Rhea	527.07	0.001	230.9
Titan	1221.87	0.0288	13455.3
Hyperion	1500.88	0.0274	1.08
Iapetus	3560.84	0.0283	180.59
Phoebe	12947.78	0.1635	0.8289

is disregarded. On the other hand, if the test particle does not fulfill any of these requirements before the end of the numerical integration at $t_{\rm end}$, the test particle is said to be a trapped particle and, in that sense, a particle of the ring. We shall see below that an additional dynamical criterion related to the stability properties of the orbit must be imposed, which accounts for the possibility of a future escape. We rely on numerical simulations to study the dynamics of the test particles.

3. Numerical results

The results presented below were obtained using a high-order Taylor's integration method (maximum order of the Taylor expansion was 28) for the numerical integration (Jorba and Zou, 2005). The absolute error of the largest of the two last terms of all Taylor expansions in every integration step, which is used to determine each step size of the integration, was fixed to $\epsilon = 10^{-21}$. The accuracy of the integrations is such that the energy and the angular momentum of Titan's Kepler motion, in absolute terms, is conserved throughout the whole integration below 2×10^{-14}.

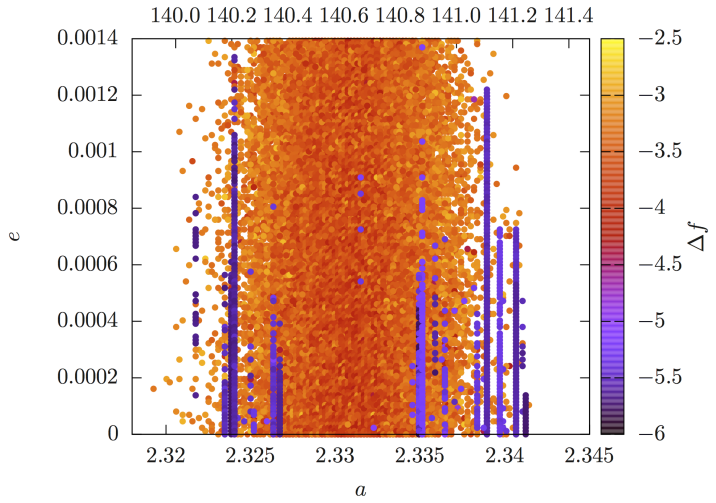

Figure 1: Projection onto the semi-major axis a and eccentricity e plane of the initial conditions of test particles that remain trapped for at least $t_{\rm end} = 2.4 \times 10^6\, T_{\rm Prom}$. The color code is the stability index Δf associated with the mean motion in logarithmic scale (see text). Notice that there are two localized regions in the $a-e$ plane, where the particles exhibit an enhancement of the stability index (blue-purple stripes). The lower a-axis is expressed in Saturn radius units R_S and the upper one is expressed in 10^3 km.

3.1. Initial conditions and trapped orbits

We first define the initial conditions for this problem. Since the model assumes independent test particles, each particle is represented by an independent initial condition of the Hamiltonian (2). The initial conditions for each test particle are fully characterized by its semi-major axis a, its eccentricity e, and two angles that define the orientation of the initial ellipse ω with respect to an arbitrary direction, the argument of pericentre, and the actual position M along the ellipse, the mean anomaly. We shall focus in the phase-space region defined by $a \in [2.318, 2.345]$, $e \in [0, 1.45 \times 10^{-3}]$, and $\omega, M \in [0, 2\pi]$. This region, when projected onto the coordinate space, spans the (planar) region between the orbits of Prometheus and Pandora. Hence, the orbital elements of the particles of Saturn's F ring are included in this phase-space region (under the assumption of planar orbits), though we emphasize that this region is not restricted only to such orbital elements. As we shall show, the dynamics of this system *selects*, through the escaping mechanism and a further stability condition, a specific subset of these initial conditions.

With regards to the initial conditions of the massive bodies, these will be fixed to an arbitrary but fixed value for all integrations. The case we have considered is rather artificial, all moons are initially aligned at their pericentre, with their orbital elements corresponding to the nominal ones (see footnote 1). As we shall show below, the results for this particular situation have a good correspondence with the observations; this illustrates the robustness of the proposed approach.

In Figure 1 we display the initial conditions for the test particles that remain trapped for at least $t_{\text{end}} = 2.4 \times 10^6$ periods of Prometheus, projected onto the semi-major axis a and eccentricity e plane. In these simulations, the orientation of the initial Kepler ellipses was varied considering 10 equally spaced values for ω for $M = 0$; the semi-major axis and the eccentricity was set on a grid of 256×256 points for each value of ω. Leaving aside the color code for the moment, which will be explained below, the results shown in this figure indicate that the trapped particles occupy a rather wide and connected region for both a and e. This statement holds for other initial values of ω and M.

These results seem deceiving at first sight: In general, the inclusion of Titan in the model promotes more extended radial excursions of the test particles. These radial excursion may induce collisions with the shepherds or escape from the region between the shepherds. However, for the integration times considered so far, the result is a wide region in the semi-major axis occupied by the trapped test particles. That is, Titan does not confine the trapped test particles to a narrow region in a, where a (narrow) ring could be located and compared with the observations.

The fact that Titan promotes more extended radial excursions without clearing out efficiently (in a short-time scale) the region between the shepherds motivates to explore the stability properties of the motion of the test particles (Benet and Jorba, 2013). We shall do so considering a variation of the frequency analysis (Laskar, 1990). To be more specific, we characterize the variation of a given frequency, or an action, along the whole integrated orbit using a stability index defined by the standard deviation of the frequency (or action) normalized by its average value. In particular, in Figure 1 we considered the stability index $\Delta f = \sigma_f / \overline{f}$ associated with the mean motion f. In terms of Δf, periodic or quasi-periodic motion implies $\Delta f = 0$. Therefore, large-enough non-zero values of Δf indicate clear departures from stable or quasi-periodic motion.

From the numerical integration for each test particle, we computed the

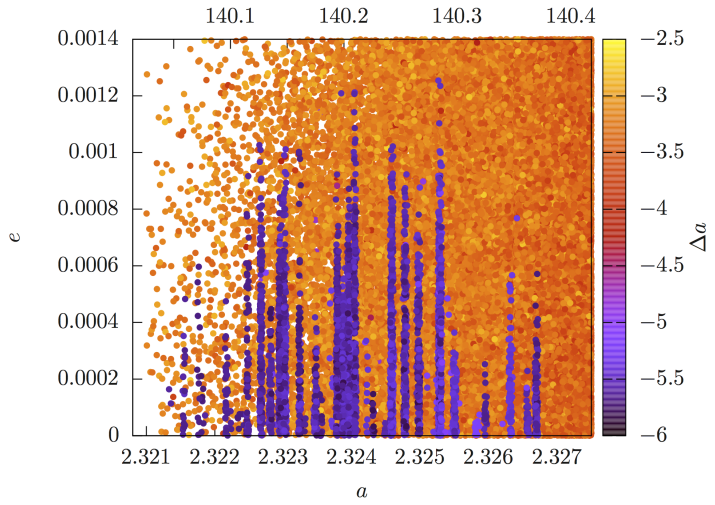

Figure 2: Projection onto the semi-major axis a (close to the region where the F ring is observed) and eccentricity e plane of the initial conditions of test particles that remain trapped at least up to $t_{\text{end}} = 3.2 \times 10^6\, T_{\text{Prom}}$. For this figure the whole M and ω domains were considered. The stability index has been coded with respect to Δa, the normalized standard deviation of a, in logarithmic scale. Note that the scales differ from those in Figure 1, and include the region with Saturn's F ring is actually observed. The lower horizontal scale is expressed R_S, and the upper one is given in 10^3 km.

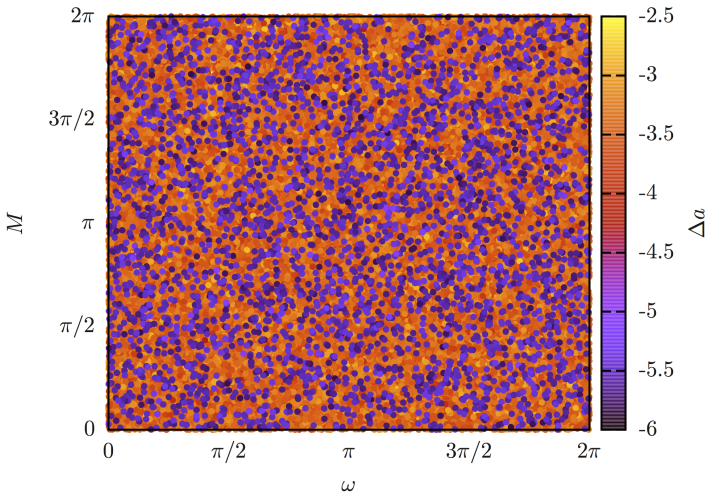

Figure 3: Projection onto the space of angles $\omega - M$ of the same initial conditions depicted in Figure 2. The distribution of stable trajectories seems quite homogeneous, indicating that that the stability index Δa (in logarithmic scale) is independent of the angular components of the initial conditions.

main frequencies every 200 revolutions of Prometheus, using a collocation method for the Fourier analysis (Gómez et al., 2010). The color code used in Figure 1 corresponds to $\log_{10}(\Delta f)$. Taking into account the color code, we note the appearance of localized stripes in the semi-major axis at certain locations, around $a \sim 2.325$, and $a \sim 2.340$. These locations are particularly stable in terms of Δf. Below we shall show, using longer numerical integrations, that a large proportion of particles whose stability index is in the orange-yellow region are escaping orbits, while a minor quantity behaves alike in the blue–purple region.

It is interesting to note that the first group of blue–purple stripes mentioned above, located around $a \sim 2.325$, is close to the nominal semi-major axis of Saturn's F ring; cf. Table 1. We shall focus on this region from now on, due to its correspondence with the nominal orbital data of Saturn's F ring. We note that in Figure 1, as well as in Figures 2, 4 and 6 displayed below, we have included an upper scale for the radial distances given in km, which may be used to compare with the nominal data. For the conversion we use $R'_S = 60330$ km, since this value is used to obtain the nominal value for $a_{\rm Fring}$ during the data reduction and fitting processes (see Bosh et al., 2002; Cooper et al., 2013; Cuzzi et al., 2014). Yet, our main interest is not on the

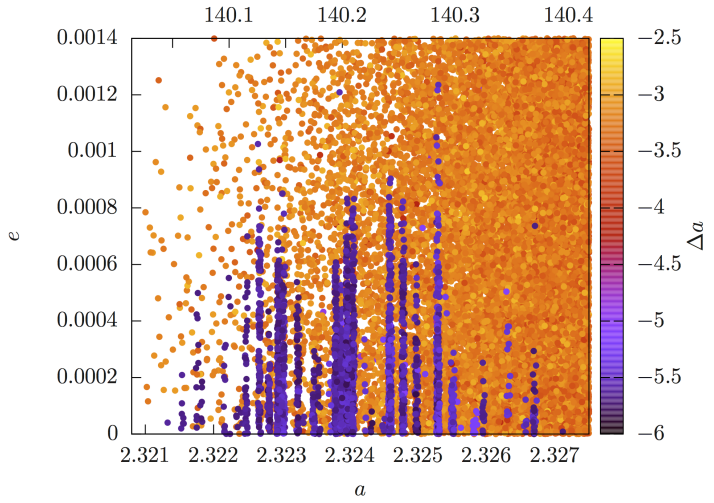

Figure 4: Same projection as in Figure 2 for test particles that stay trapped at least up to $t_{\rm end} = 6.0 \times 10^6\, T_{\rm Prom}$. Notice the appearance of a white background indicating that some test particles have escaped. The majority of the initial conditions of the escaping test particles have stability indexes in the orange-yellow region. The lower horizontal scale is expressed R_S, and the upper one is given in 10^3 km.

correspondence to this value but on a generic mechanism that yields a narrow ring. We note though that, using this factor yields a better comparison of our results with the nominal data than using the value of R_S from Seidelmann et al. (2007) which we used to scale out the physical units in our numerical simulations. The differences in the scale are below 0.2% due to the difference in the R_S values. For $a \sim 2.324$, this difference amounts to ~ 140 km.

Figure 2 illustrates the projection of the trapped orbits around this region for longer integrations ($t_{\rm end} = 3.2 \times 10^6\, T_{\rm Prom}$); the initial conditions are taken from the whole M and ω domains. In this case, the stability index has been computed with respect to Δa, i.e., with respect to the normalized standard deviation of the semi-major axis of the test-particle's orbit, which was calculated using an averaging extrapolating method to achieve rapid convergence (Luque and Villanueva, 2014). Clearly, Δa is a measure of the radial excursion of the test particle. Again, groups of blue–purple stripes appear localized around certain values of the semi-major axis. Regarding the angular correlations of the trapped test particles, Figure 3 shows that the initial angles M and ω do not display any prominent structure with respect to the stability index.

In Figure 4 we display the projection into the $a - e$ space of the initial conditions that remain trapped at least up to $t_{\rm end} = 6.0 \times 10^6\, T_{\rm Prom}$. The structure resembles that of Figure 2, except that many initial conditions that were trapped in Figure 2 have now escaped. The vast majority of the escaped particles correspond to test particles in the orange-yellow region of the stability index Δa displayed in Figure 4. An example of this can be easily noticed by the white regions appearing on the middle-left of Figure 4, which were before occupied mainly by orange-yellow dots.

The last observation confirms the naive expectation that only the most stable particles will remain trapped, in the sense that their radial excursions are strongly limited (Benet and Jorba, 2013; Cuzzi et al., 2014). While this statement may sound trivial, we emphasize that the Hamiltonian (2) is explicitly time-dependent, and its time dependence reflects the dynamics of the N-body Hamiltonian. Moreover, we recall that the shepherd moons move along seemingly chaotic orbits (Poulet and Sicardy, 2001; French et al., 2003; Goldreich and Rappaport, 2003a,b).

3.2. Statistical properties of the stability index and rings

Figure 5 displays the frequency histograms of the logarithm of Δa for the trapped test-particles considering the two distinct integration times. The empty histograms corresponds to the data used in Figure 2 for $t_{\rm end} = 3.2 \times 10^6\, T_{\rm Prom}$, and the filled histograms to Figure 4 for $t_{\rm end} = 6.0 \times 10^6\, T_{\rm Prom}$. From Figure 5, we observe that the trapped test particles clearly display two well-separated scales according to Δa. These scales correspond, for a test particle with $a \simeq 2.324$, to radial excursions in the kilometer scale for $\Delta a \lesssim 10^{-5}$ (blue-purple region), or from tens to hundreds of kilometers for $\Delta a \gtrsim 10^{-4}$ (orange-yellow region).

A test particle moves along a perturbed precessing ellipse with a limited radial excursion. Titan's eccentric orbit promotes more extended radial excursions (see Appendix A) which may be amplified by local encounters with the shepherd moons (c.f. Figure 8 in Cuzzi et al., 2014). These combined perturbations create conditions which result in a larger change in the semi-major axis and eccentricity. The net result is a more extended radial excursion of the test-particle orbit, and hence a comparatively large value of Δa, which could lead to the escape of the test particle. Test particles that somehow experience these large radial excursion but remain trapped at time $t_{\rm end}$, correspond to the orange–yellow points in Figures 2 and 4, i.e., to somewhat large values of Δa. The blue-violet dots in those figures correspond to

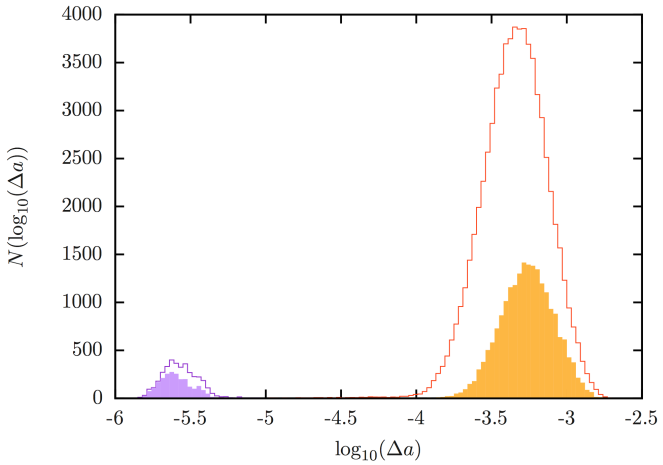

Figure 5: Frequency histogram of $\log_{10}(\Delta a)$ corresponding to the data used in Figure 2 for $t_{\rm end} = 3.2 \times 10^6\, T_{\rm Prom}$ (empty histograms) and to the data of Figure 4 for $t_{\rm end} = 6.0 \times 10^6\, T_{\rm Prom}$ (filled histograms). Note that the number of initial particles with larger stability index (orange-yellow region) shrinks in a larger proportion than the region of smaller Δa (blue-purple region).

test particles that have experienced very few or no abrupt changes in their semi-major and eccentricity, and therefore, the associated Δa value remains very small. Figure 5 shows that the test-particles in the orange-yellow region are more prone to abandon the region between the shepherds than those in the purple-blue region.

It is only matter of time before test particles in the orange–yellow region will eventually escape. This statement does not preclude that test particles with very small values of Δa (measured at a given time) also escape, though it suggests that the typical time scale needed for them to escape may be much longer. Note that, as soon as there is an important radial excursion, the value of Δa increases, which reflects the instability of the motion in the radial direction.

The structure of Figure 5 suggests, on dynamical grounds, to filter the trapped test particles according to their stability index, which in a way mimics performing longer time integrations. We thus retain as the actual particles of the ring those whose stability index is small enough. In particular, we consider that the ring particles satisfy $\Delta a < 10^{-5}$. Using this dynamical filtering, in Figure 6 we present the projection of the ring particles onto the $X - Y$ space using a polar representation; Figure 6(a) corresponds to the

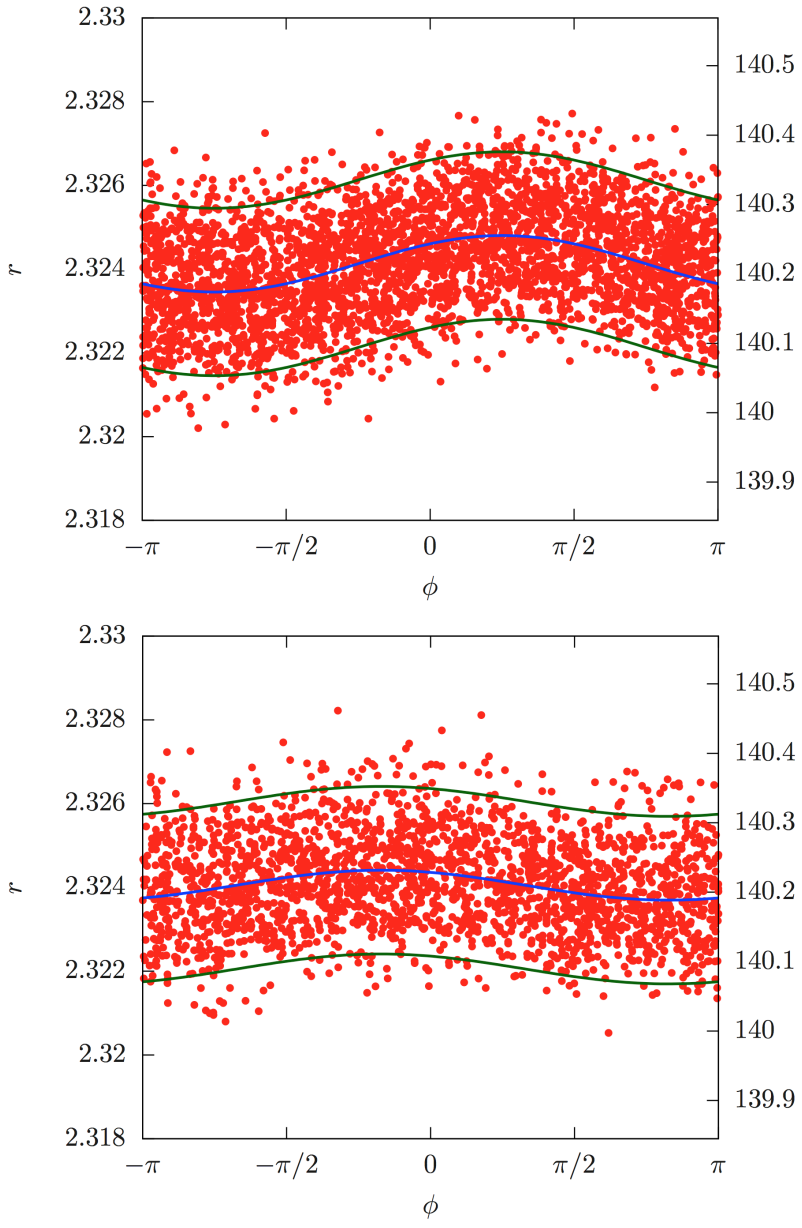

Figure 6: Snapshots of the ring particles, in polar coordinates, after the dynamical filtering at (a) $t = 3.2 \times 10^6\, T_{\rm Prom}$ and (b) $t = 6.0 \times 10^6\, T_{\rm Prom}$. In both frames, the blue middle line corresponds to the Keplerian ellipse fit considering all the particles of the ring; the outer green lines are the same ellipse shifted upwards or downwards by $\delta r = 0.002 \approx 120.5\,$km, and permit to obtain a rough estimate of the width of the ring. The left vertical scale is given in R_S units, and the right one in 10^3 km.

snapshot taken at $t = 3.2 \times 10^6\, T_{\rm Prom}$ and 6(b) to the snapshot taken at $t = 6.0 \times 10^6\, T_{\rm Prom}$, respectively. The ring obtained in each frame is narrow and slightly eccentric.

The rings of Figure 6 have a well-defined collective orientation, despite of the fact that each ring particle has independent and randomly chosen initial conditions; this is another consequence of the dynamical filtering employed, i.e., to the radial stability criterion. This collective orientation suggests that the ring displays apse alignment, though we have not proven it; we shall come back to this later. An estimate of the instantaneous orbital elements is obtained by fitting a Keplerian ellipse of the form

$$r = \frac{a(1-e^2)}{1 + e\cos(\phi - \phi_0)}, \tag{3}$$

to all particles of the ring at a given time. For the data in Figure 6(a) we obtain for the semi-major axis $a_{\rm fit} \approx 2.3241 \approx 140213$ km and the eccentricity $e_{\rm fit} \approx 2.9 \times 10^{-4}$, using $\phi_{0\rm fit} \approx -3\pi/4$. For the data of Figure 6(b) we obtain essentially the same semi-major axis (differences appear beyond the fourth decimal, yielding 140210 km) and $e_{\rm fit} \approx 1.5 \times 10^{-4}$ using $\phi_{0\rm fit} \approx 2.6$. The corresponding fits are displayed in Figure 6 by the (middle) blue lines. The outer green lines correspond to the same fitted ellipse shifted upwards and downwards by $\delta r = 0.002$, which is approximately equivalent to 120.5 km. These limits include over 90% of the ring particles in each snapshot. Hence, these curves provide a rough estimate of the width of the ring, which is given by $2\delta r \approx 0.004 \approx 241$ km.

Note that, the surface density of test particles decreases very fast. In more quantitative terms, in Figures 7 we present the histogram of ring particle radial positions corresponding to the rings of Figures 6. The red curve in the histograms corresponds to a Gaussian distribution that uses the mean and the variance computed from the radial positions. This shows that the surface density of ring particles decays at least as a Gaussian. It is in this sense that we state that the ring obtained displays sharp edges.

The semi-major axis of the ring $a_{\rm fit}$ given above is in correspondence with the observations for Saturn's F ring, namely, $a_{\rm Fring} = 140221.6$ km $\approx 2.324243...R'_S$ (Bosh et al., 2002; Cooper et al., 2013). Differences exist though, that are attributed to the simplicity of the model. With respect to the width, we note that our definition is similar to the definition of the core employed by French et al. (2012). Our estimate for the width is consistent with the Voyager 1 results, though it is about half of the mean-width

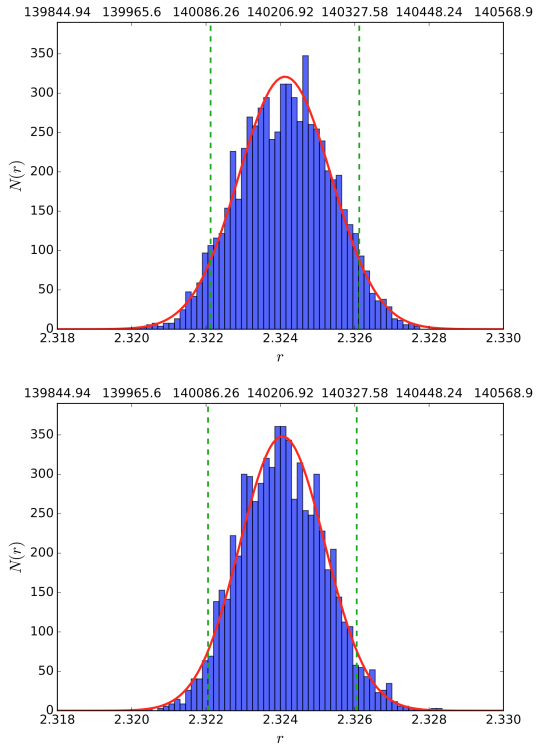

Figure 7: Frequency histograms of the radial positions of the ring particles of Figures 6 at (a) $t = 3.2 \times 10^6\, T_{\rm Prom}$ and (b) $t = 6.0 \times 10^6\, T_{\rm Prom}$. The red curves correspond to Gaussian distributions with the same mean and variance of the data; these curves are included as a guide for the tails of the distribution, which leads us to conclude that the tails have at least a Gaussian decay. The vertical lines correspond to the shifts by δr used to estimate the width of the ring (green lines in Figures 6). The lower horizontal axis scale is given in R_S, and the upper one in km.

obtained from the photometric analysis of Cassini's data, which is wider than Cassini's occultation data (see French et al., 2012). It is also consistent with the simulations performed by Cuzzi et al. (2014, cf. figure 18), and the total extent of the F ring reported in Bosh et al. (2002, see the discussion of Sect. 6 and Fig. 7). Yet, the value largely overestimates the width associated with the core, which is in the range of $1 - 40$ km. Note that, while we have obtained an eccentric ring, the values of the eccentricity obtained are about an order of magnitude smaller than the observations (Bosh et al., 2002; Albers et al., 2012; Cooper et al., 2013). This may be a consequence of neglecting the larger bodies in the ring, collisions among the ring particles, or to the overall simplicity of our model.

Similar to the fits based on Eq. (3) performed above for the snapshots in Figures 6, in Figures 8 we plot the fitting parameters $a_{\rm fit}$, $e_{\rm fit}$ and $\phi_{0{\rm fit}}$, as a function of time, for three data sets. Each data set spans a time window of 200 time-units at $t_{_{\rm end}} = 1.6\times10^6\, T_{\rm Prom}$ (blue data), $t_{_{\rm end}} = 3.2\times10^6\, T_{\rm Prom}$ (red data) and $t_{_{\rm end}} = 6.0\times10^6\, T_{\rm Prom}$ (green data). The fitted parameters display spurious short-time oscillations, whose periodicity is related to the period of Prometheus in this stroboschopic map ($200/(2\pi) \approx 32$). For $a_{\rm fit}$ and $e_{\rm fit}$ we observe a longer time-scale variations, which we attribute to secular effects. Note that, while this secular time-scale is clear for $e_{\rm fit}$ in each individual data set, for $a_{\rm fit}$ it appears only by comparing the three data sets.

Regarding $\phi_{0{\rm fit}}$, the slope of the linear trend is an estimate of the apse-precession rate. We have fitted each data set to a straight line (for the green data, this was done using the last 20 points). The average slope is an estimate for the precession rate; the black lines displayed in Figure 8(c) have this average slope. We obtain $\dot{\varpi}_{\rm fit} \approx 0.003867$ rad/time-units, which corresponds to 2.27105 deg/day. This estimate can be compared with the nominal precession rate of the F ring which corresponds to $\dot{\varpi}_{\rm Fring} = 2.7001$ deg/day (Bosh et al., 2002). The difference can be attributed to the simplicity of our model, in particular the fact that we only considered the J_2 zonal harmonic. The similarity in the slopes of the three data sets gives further support to the claim that the ring displays apse alignment.

While our results show certain agreement with the observations, we should emphasize that this *a posteriori* consistency does not prove the dynamical filtering that we have employed. It is through longer numerical integrations, or a thorough understanding of the relevant invariant phase space structures, that we can prove if the filtered particles indeed escape and if the retained ones do not. With this proviso in mind, the comparison with the observations

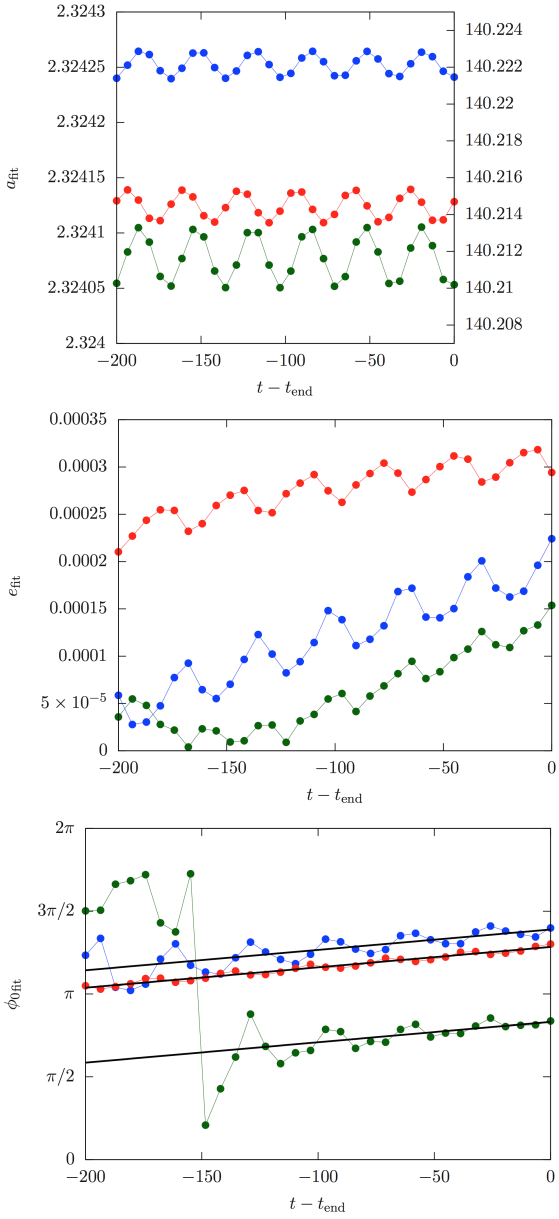

Figure 8: Ring fitting parameters (a) $a_{\rm fit}$, (b) $e_{\rm fit}$ and (c) $\phi_{0\rm fit}$ as a function of time, spanning 200 time-units ($200/(2\pi)\,T_{\rm Prom}$) close to three epochs: $t = 1.6\times10^6\,T_{\rm Prom}$ (blue data), $t = 3.2\times10^6\,T_{\rm Prom}$ (red data) and $t = 6.0\times10^6\,T_{\rm Prom}$ (green data). The left vertical scale of (a) is given in R_S and the right one in 10^3 km. The black straight-lines in (c) correspond to a precession rate $\dot{\varpi}_{\rm fit} \approx 0.003867$ rad/time-units.

is rewarding.

3.3. Orbital resonances

So far, we have shown numerically that, among the trapped particles (up to $6.0 \times 10^6\, T_{\rm Prom}$), the most stable ones according to the stability indicator Δa yield a narrow and eccentric ring. Here, we shall consider the orbital resonance structure in the region where the ring is located ($2.321 < a < 2.3275$, c.f. Figure 4), considering all Saturn moons of our model, the test particle and the J_2 zonal harmonic of Saturn.

We are interested in the semi-major axis a of test particles that satisfy a resonance condition (Morbidelli, 2002), which can be written as

$$\sum_{i=1}^{4} \left[k_i \dot{\lambda}_i - l_i \dot{\varpi}_i\right] = \sum_{i=1}^{4} \left[k_i f_i + (k_i - l_i)\dot{\varpi}_i\right] = 0. \qquad (4)$$

Here, all k_i and l_i are integer coefficients, $\dot{\lambda}_i = f_i + \dot{\varpi}_i$ is the rate of change of the mean longitude, f_i and $\dot{\varpi}_i$ correspond to the mean motion and the apsidal precession rate of Prometheus, Pandora, Titan and the test particle, for $i = 1, 2, 3, 4$ respectively. We shall restrict ourselves to consider orbital resonances with $\sum_i |l_i| \leq 1$ (and $k_4 \neq 0$) only, since all involved eccentricities are quite small, and the amplitude of the Fourier coefficient corresponding to the resonance is at least proportional to $e_i^{|l_i|}$, with e_i the eccentricity of the i-th body (Murray and Dermott, 2000).

We locate the resonances as follows: We fix the frequencies for the moons (from our numerical integrations, though similar results are obtained using the nominal data) and use two fixed intervals, $\mathcal{I}_{f_4}$ and $\mathcal{I}_{\dot{\varpi}_4}$, for the possible frequencies of the particle of the ring. These intervals contain the possible values of the frequencies that are compatible with a semi-major axis a_4 in the interval $\mathcal{I}_{a_4} = [2.321,\ 2.3275]$; these intervals are given by $f_4 \in \mathcal{I}_{f_4} = [0.990365, 0.994541]$ and $\dot{\varpi}_4 \in \mathcal{I}_{\dot{\varpi}_4} = [4.470, 4.498] \times 10^{-3}$. Then, for a given set of integer coefficients k_i and l_i that satisfy d'Alambert's relation, $\sum_i (k_i - l_i) = 0$ (Morbidelli, 2002), we check if zero is contained in the interval obtained from Eq. (4). If zero is not in the interval, we conclude that there is no resonance with the specific integer coefficients tested. If the resulting interval does contain zero, we use Newton's method to compute the test particle's semi-major axis that corresponds to the zero of Eq. (4) together with the associated resonant frequencies. To first order in J_2, the mean-motion and the horizontal epicyclic frequency in terms of the semi-major

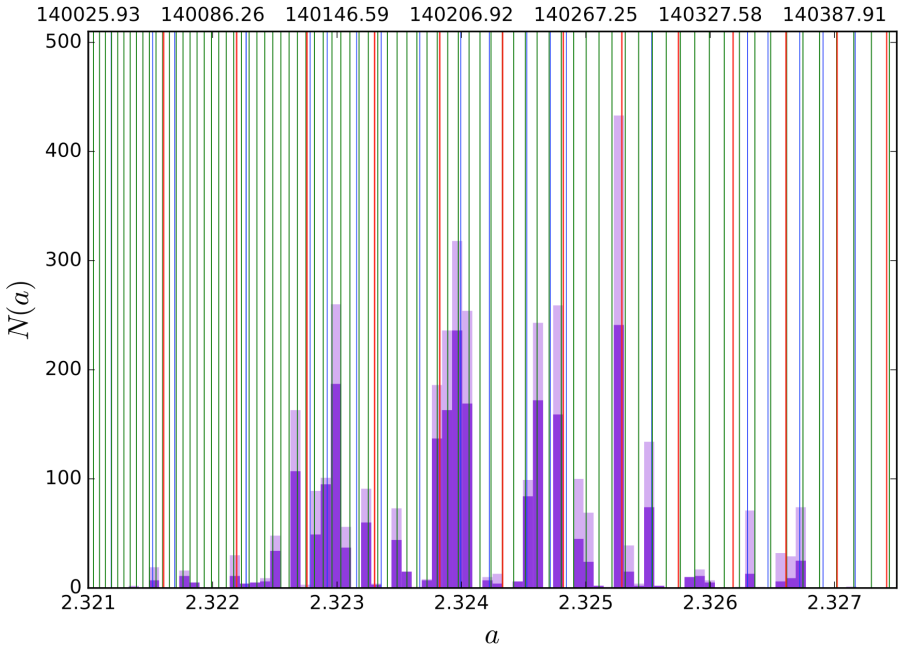

Figure 9: Frequency histogram (using 80 bins) of the semi-major axis of the ring particles ($\Delta a < 10^{-5}$) for the the numerical integrations up to $t_{\rm end} = 3.2 \times 10^6\, T_{\rm Prom}$ (light purple histogram) and $t_{\rm end} = 6.0 \times 10^6\, T_{\rm Prom}$ (dark purple histogram). The vertical lines indicate the location of some resonances: green lines correspond to Prometheus' outer Lindblad and co-rotation resonances, red lines to Pandora's inner Lindblad and co-rotation resonances, and blue lines to low-order orbital resonances involving the mean-motion of both shepherds and the ring-particles only. The lower horizontal axis scale is given in R_S and the upper one in km.

axis are given by (Lissauer and Cuzzi, 1982)

$$n^2 = \frac{\mathcal{G}m_0}{a^3}\Big[1 + \frac{3}{2}J_2\Big(\frac{R_S}{a}\Big)^2\Big], \tag{5}$$

$$\kappa^2 = \frac{\mathcal{G}m_0}{a^3}\Big[1 - \frac{3}{2}J_2\Big(\frac{R_S}{a}\Big)^2\Big]. \tag{6}$$

From these frequencies, the apsidal precession rate is obtained, $\dot{\varpi} = n - \kappa$.

In Figure 9 we show the histogram of the ring particle's semi-major axis, using the numerical integrations displayed in Figures 2 (light purple) and 4 (dark purple). The histograms have been constructed using 80 bins in the semi-major axis interval $\mathcal{I}_{a_4}$. The histograms show the decrease in the ring particle number for the longer integrations mentioned above.

The vertical lines displayed in Figure 9 correspond to different resonances found within the semi-major interval of interest; Figures 10 show the same results using 400 bins in the construction of the histogram on $\mathcal{I}_{f_4}$; note that Figure 10(b) spans the region where the nominal semi-major axis of the F ring is located. With the method described above, we located all low-order resonances defined by the condition $\sum_i(|k_i| + |l_i|) \leq 40$. The maximum order was set to 40 for convenience; low order resonances are often preferred since the amplitude of the Fourier coefficients decreases with the order of the resonance. The blue vertical lines in Figures 9 and 10 are, among these low-order resonances, those that only involve the mean motions, i.e., $\sum_i |l_i| = 0$. It turns out that, up to the order calculated, these resonances involve the mean motion of both shepherd moons and the particle of the ring.

In addition to those resonances, the vertical green lines correspond to Prometheus' outer Lindblad and co-rotation resonances, $-j_1 f_1 + (j_1+1)f_4 + \dot{\varpi}_4 = 0$ and $-j_1 f_1 + (j_1+1)f_4 + \dot{\varpi}_1 = 0$, respectively, with $102 \leq j_1 \leq 179$. Likewise, the red lines correspond to Pandora's inner Lindblad and co-rotation resonances, $-(j_2+1)f_2 + j_2 f_4 - \dot{\varpi}_4 = 0$ and $-(j_2+1)f_2 + j_2 f_4 - \dot{\varpi}_2 = 0$, respectively, with $50 \leq j_2 \leq 62$. These pairs of resonances lie so close together that it is difficult to distinguish them; only few doublets of Pandora's resonances are apparent in Figures 10. During the computation of these resonances, we noticed the proximity of other resonances with nearby values of j_1 (j_2) which involved the mean-motion of Prometheus (Pandora), the mean-motion of the particle of the ring and the apse precession of Pandora (Prometheus), or even Titan. While the former lie very close to Prometheus (Pandora) outer (inner) Lindblad and co-rotation resonances, those that involve Titan's precession rate are well separated. In Figures 10 we have included the resonances of the form $-j_1' f_1 + (j_1'+1)f_4 + \dot{\varpi}_3 = 0$ and $-(j_2'+1)f_2 + j_2' f_4 - \dot{\varpi}_3 = 0$, that involve Titan's precession rate, as dotted-green and dotted-red vertical lines, respectively. The latter are the only resonances displayed in Figures 9 and 10 that involve Titan; some of them may be relevant for the location of the ring, as we point out below. There are other resonances in this region which also involve Titan; yet, those resonances are three-body resonances, and their significance is not clear.

As shown in Figures 10, many of the accumulation regions of the ring particles can be associated with some resonances, and mostly with Prometheus' outer Lindblad and co-rotation resonances (green lines). We note that, to each such pair of resonances there is, within the same region of ring-particle accumulation, a nearby resonance of the form $-j_1' f_1 + (j_1'+1)f_4 + \dot{\varpi}_3 = 0$

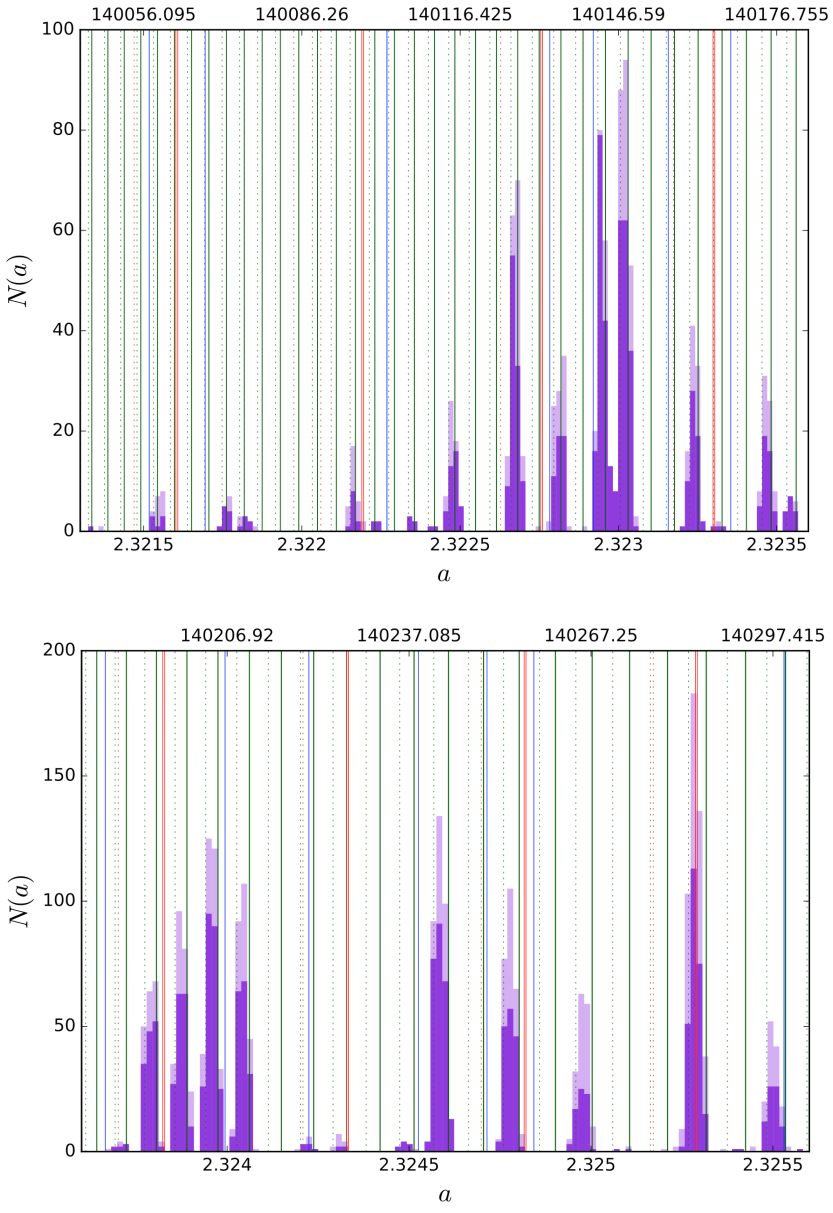

Figure 10: Details of two regions of Figure 9, using 400 bins to construct the histograms; note that the vertical scales differ. Some resonances are located at the gaps between two nearby regions of ring particle accumulation; most Pandora's inner Lindblad and co-rotation resonances (red lines) lie in these gaps. Some of Prometheus' outer Lindblad and co-rotation resonances (green lines), and resonances involving Prometheus' mean-motion and Titan's apse precession (dotted green lines), appear within the same region of accumulation of ring particles. The lower horizontal scales are given in R_S and the upper ones in km.

which involves Titan's apse precession. The most prominent peak, c.f. Figure 10(b), located at $a = 2.32529... \approx 140284.7$ km can be associated with Pandora's inner Lindblad and co-rotation resonances with $j_2 = 57$; these resonances are flanked by Prometheus' outer Lindblad and co-rotation resonances with $j_1 = 119$ and their partner involving Titan's apse precession ($j_1' = 120$). Other Pandora's inner Lindblad and co-rotation resonances (red lines) as well as most low-order three-body orbital resonances (blue lines) appear in gaps between regions of accumulation of ring particles. This is illustrated in Figure 10(b) by two of the gaps in the accumulation region close to the semi-major axis 2.324. One exception to this is the three-body resonance $-11f_1-6f_2+17f_4 = 0$, which is located around $a \sim 2.3263 \approx 140345.7$ km; cf. Figure 9. The region close to $a = 2.3255 \approx 140297.4$ km seems to be related to the proximity of the low-order three-body resonance $-2f_1 - f_2 + 3f_4 = 0$ and Prometheus' outer Lindblad and co-rotation resonances (with $j_1 = 117$), including the corresponding partner resonance involving Titan's apse precession ($j_1' = 118$).

From the observations described above, we may conclude that the accumulation regions where the ring particles are found can be essentially associated with Prometheus' Lindblad and co-rotation resonances and their companion resonance which involves the precession rate of Titan. Yet, not all Prometheus' outer Lindblad and co-rotation resonances coincide with a region of accumulation of ring particles. Similarly, Pandora's inner Lindblad and co-rotation resonances as well as the low-order three-body resonances seem to be related to gaps rather than regions of accumulation of test particles, but exceptions exist. If these resonances somehow induce dynamical instabilities, we may expect that as time passes the ring particles found in the accumulation regions crossed by these resonances will escape; this assertion may be proved by considering even longer integrations. The explicit mechanism is not clear at this point.

4. Summary and conclusions

In this paper we have studied a simple model for the location of Saturn's F ring. The model includes the gravitational influence of Saturn with its J_2 zonal harmonic, Prometheus, Pandora and Titan, on massless point particles, and assumes that the dynamics takes place in the equatorial plane. The initial conditions of the test particles are randomly chosen, imposing only that they are within the region between Prometheus and Pandora at the initial

time of our simulations. We have computed accurate long-time numerical integrations that show that there is a wide region, in the initial condition space, of test particles that stay in the region between Prometheus and Pandora, i.e., that do not escape from that region nor collide with the shepherds up to the final integration time. Among these trapped test particles, we uncovered a clear scale separation according to the value of the dynamical stability indicator Δa. The most stable ones, which correspond to $\Delta a < 10^{-5}$ with a maximum excursion $\lesssim 1.5$ km, are located around specific values of the semi-major axis, defining localized stripes in the semi-major axis and eccentricity plane. Retaining only the most stable test-particles, i.e., those particles whose dynamics do not display extended radial excursions, their projection onto the $X - Y$ plane forms a narrow eccentric ring which, as time passes, maintains a collective elliptic shape.

Fitting the whole ring to a Keplerian ellipse yields a semi-major axis that is comparable to the observations. The fitted value for the eccentricity is about an order of magnitude smaller, and the width of the ring is ~ 241 km, comparable to some observations and simulations, but largely overestimating a core of $1 - 40$ km. Using various snapshots spanning ~ 30 periods of Prometheus at different epochs, we obtain consistent values for the apse precession rate, which are somewhat smaller than the observations, but of the same order of magnitude. In that sense, the ring obtained displays apse alignment. We emphasize that, in the context of our simulations, it cannot be attributed to the mass of the ring; the actual mechanism that yields apse alignment remains unclear.

Note that the actual value for the semi-major axis obtained from fitting the rings of Figures 6 to a Keplerian ellipse, $a_{\rm fit} \approx 2.3241\, R_S$, does not match the location of any of the (most populated) ring-particle accumulation regions; c.f. Figure 10. This remark is trivial, in the sense that the fitting procedure is collective and involves the position of all ring particles with equal weight. Yet, it emphasizes the fact that the whole set of stable trapped ring particles has to be considered. This indicates also that orbital fits of individual objects (which a priori are located within a ring-particle accumulation region) may not match the fitting parameters for the ring. This agrees with results of Cooper et al. (2013) that show that local variability of the ring is compatible with a consistent solution for the whole ring. It also suggests that the orbital elements fitted to some bright features that have been observed, represent a region where stable ring-particles accumulate.

Cuzzi et al. (2014) addressed similar questions considering a more real-

istic model (14 Saturn moons and including J_2, J_4 and J_6 Saturn's zonal harmonics) and shorter time integrations, up to 20000 Prometheus periods. As a measure of the stability of test particles they considered the semi-major axis RMS deviation during the time spanned by the integration. In their Figure 9, they obtain a one to one correspondence of the trapping stripes with the Prometheus' outer Lindblad and co-rotation resonances. (The aim of that figure was to show the robustness of the calculations with respect to changes of the zonal harmonics.) While we also find an association of the regions of ring-particle accumulation to such Prometheus resonances, our results show that not all Prometheus resonances are associated with a ring-particle accumulation region. In this case, the difference is attributed to the facts that Pandora was not included in those calculations and the integrations are rather short (5000 Prometheus periods for their Fig. 9). Other calculations that include Pandora (Cuzzi et al., 2014, Figures 14–16, up to $20000\,T_P$) show that Pandora's resonances influence the stability of the tests particles, rendering them less stable, i.e., larger semi-major axis RMS deviations are observed. Our results are similar with respect to the semi-major axis, though Δa defines naturally the stability through a scale separation. We also observe more sensitivity with respect to the eccentricity of the ring particles, which in our case are smaller than the values considered in Cuzzi et al. calculations; this may be related to the much longer integration times we considered. Despite of the specific differences of the models and methods, the results are consistent. We interpret this as the robustness of the approach.

The quantity Δa seems to be a good dynamic indicator to address if a test particle escapes or not, depending on whether or not its value is large enough. In our numerical results, there is a natural scale separation defined by the statistics of Δa for the trapped particles. However, some ring-particles with a small value of Δa may escape at later times. In our model, escape is the result of the accumulation of small radial excursions due to the combined action of the moons considered in the model, which are enhanced by impulsive encounters due to the proximity of the shepherd moons.

The ring particles accumulate in regions which seem related to occurrence of orbital resonances, typically involving Prometheus' outer Lindblad and co-rotation resonances, though not all such resonances are associated with regions of accumulation; similar results were obtained by Cuzzi et al. (2014). We also considered the location of other resonances. Low-order resonances in the region of the ring involve the mean motions of both shepherds and

the particle of the ring; these resonances, as well as most of Pandora's inner Lindblad and co-rotation resonances, seem related to gaps where the radial excursions are large enough, though some match ring-particle accumulation regions.

We emphasize that we have only found a possible association between resonance locations and the occurrence of accumulation regions and gaps, without providing an explanation that links the specific resonance to the actual dynamics. Cuzzi et al. (2014) propose an "anti-resonance" mechanism to explain the suppression of radial diffusion. In essence, the idea is that at certain locations (m-th Prometheus' outer Lindblad and co-rotation resonances, with $m \gg 1$) radial excursions promoted by perturbations from a close approach of Prometheus to the ring, are counterbalanced by the next close approach of this shepherd. Cuzzi et al. (2014) remark that the condition to suppress radial diffusion within the antiresonance mechanism is equivalent to the empirical commensurability $f_{\rm Prom} - f_{\rm Fring} \approx 2\dot{\varpi}_{\rm Fring}$ noted by Cooper et al. (2013). While this mechanism is physically appealing, the fact that it is equivalent to the empirical commensurability which *does not* satisfy d'Alambert's relation, suggests that something is still missing. In our analysis we have observed that close to Prometheus' outer Lindblad and co-rotation resonances, resonances involving the same (Prometheus and the ring particle) mean-motions but that the precession rate of Pandora or Titan, in particular the latter, seem to be relevant to define the narrow regions where the ring particles accumulate, though the actual mechanism is not clear. It is tempting to consider these resonances to complete the anti-resonance mechanism; this is left for the future.

Our model is rather simple and does not include many important contributions for a realistic comparison with the F ring. The role of Titan, as displayed by the resonance structure, seems marginal; yet, it influences the actual location and order of Prometheus' resonances (Cuzzi et al., 2014), and some resonances involve, which somehow makes it relevant. While Titan promotes radial excursions, it seems unable to clear all trapped unstable particles in a short-time scale; in particular, the region beyond the location of the F ring. Interactions with other moons or ring-particle collisions may contribute to this aspect. A point to be emphasized is that the occurrence of narrow rings does not require very specific scenarios with regards to the parameters, but certain stability conditions.

Acknowledgments

We would like to acknowledge financial support provided by the projects IG–100616 (PAPIIT, UNAM), SC15-1-IR-61-MZ0 and SC16-1-IR-54 (DGTIC, UNAM), the spanish grant MTM2015-67724-P and the catalan grant 2014 SGR 1145. LB expresses his gratitude to the Marcos Moshinsky Foundation for the financial support through a "Cátedra de Investigación 2012". It is our pleasure to thank Carles Simó for his encouragement, valuable comments and discussions. We would also like to thank the careful review, criticism and comments from Carl D. Murray.

Appendix A. Numerical simulations with and without Titan

Here, we present some numerical results to justify the introduction of Titan and show that it promotes radial excursions for those test particles not located within the ring-particle accumulation stripes. To this end, we consider similar integrations as described before, including or not the gravitational influence of Titan. The time integrations extend up to $t_{\rm end} = 1.6 \times 10^6\, T_{\rm Prom}$, and the initial conditions are set in two small semi-major axis regions spanning $\delta a \approx 66.4$ km; the remaining test-particle orbital elements are set as before. The first region ($a \sim 2.32475 \approx 140252.2$ km) contains stable stripes where ring particles accumulate, i.e., some particles belonging to the ring of Figures 6. The second region covers larger values of the semi-major axis ($a \sim 2.33135 \approx 140650.3$ km) which displays trapped particles, with few of them being stable according to our criterion ($\Delta a < 10^{-5}$). Note that $t_{\rm end}$ in these integrations is shorter than those considered in Figures 2 and 4; we thus expect that the particles in the second region satisfying the stability criterion will eventually display some instabilities.

In Figures 11, we present the frequency histograms of $\log_{10}(\Delta a)$ corresponding to the two intervals of semi-major axis described above; the histograms of simulations that include Titan correspond to the filled ones, while those without it are the empty ones. Figure 11(a) illustrates the results for the first region defined above. Noticeably, there are more particles trapped when Titan is not included in the simulations, though about the same number of particles that fulfill the stability criterion. In turn, Figure 11(b) displays the results for the semi-major axis region around $a \sim 2.33135 \approx 140650.3$ km. In this case, we find about the same number of trapped and ring-particles, seemingly independently of Titan's presence, though marginally more for

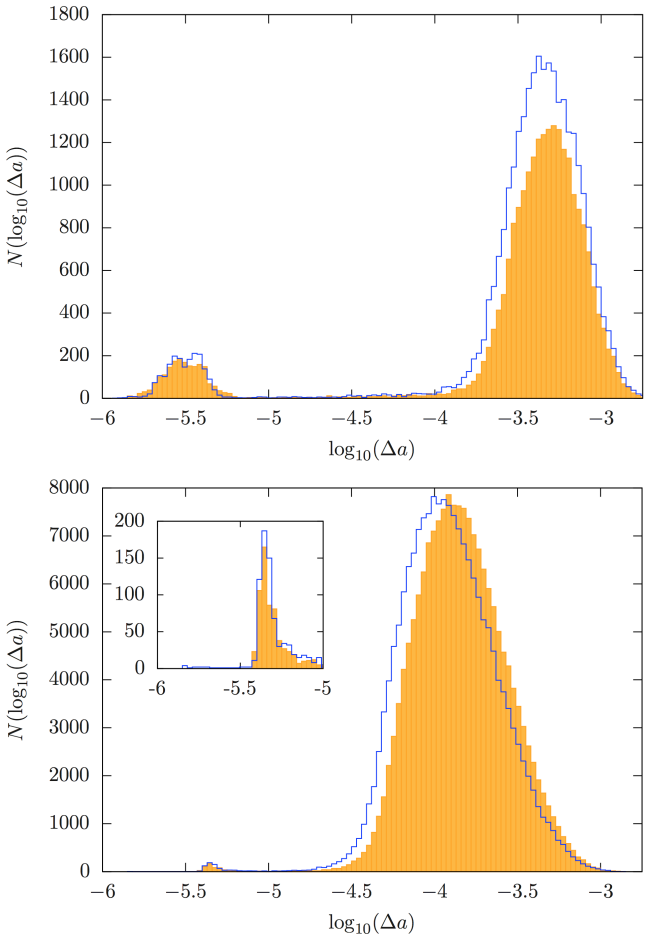

Figure 11: Frequency histogram of $\log_{10}(\Delta a)$ for two regions of the semi-major axis for integrations up to $t_{\rm end} = 1.6 \times 10^6\, T_{\rm Prom}$. Filled histograms correspond to simulations that include Titan, the empty ones are without it. (a) Semi-major axis region around $a \sim 2.32475 \approx 140252.2$ km, which contributes to the ring. (b) Semi-major axis region around $a \sim 2.33135 \approx 140650.3$ km; the inset shows an enlargement for test particles satisfying the stability criterion. Note that the vertical scales are different.

the simulations that do not include it. Notice that for the trapped particles with $\Delta a > 10^5$, the histograms without Titan (empty histograms) are slightly shifted to the left. That is, trapped particles are more stable in the simulations that do not include Titan.

These results show that Titan indeed promotes radial excursions for particles not satisfying our stability criterion. For semi-major axis in the region where the accumulation stripes are found, Titan's inclusion allows a more efficient escape mechanism. Moreover, the ring-particle accumulation regions are slightly shifted, as noted by Cuzzi et al. (2014). For larger values of the semi-major axis, the presence of Titan induces instabilities, though not enough strong to swipe the trapped particles away.

References

References

Albers, N., Sremčević, M., Colwell, J. E., Esposito, L. W., 2012. Saturn's F ring as seen by Cassini UVIS: Kinematics and statistics. Icarus 217, 367–388.

Attree, N. O., Murray, C. D., Cooper, N. J., Williams, G. A., 2012. Detection of Low-velocity Collisions in Saturn's F Ring. ApJ 755, L27.

Attree, N. O., Murray, C. D., Williams, G. A., Cooper, N. J., 2014. A survey of low-velocity collisional features in Saturn's F ring. Icarus 227, 56–66.

Barbara, J. M., Esposito, L. W., 2002. Moonlet Collisions and the Effects of Tidally Modified Accretion in Saturn's F Ring. Icarus 160, 161–171.

Benet, L., Jorba, A., 2013. Numerical Results on a Simple Model for the Confinement of Saturn's F Ring. In: Ibáñez, S., Pérez del Río, J. S., Pumariño, A., Rodríguez, J. A. (Eds.), Progress and Challenges in Dynamical Systems. Vol. 54 of Springer Proceedings in Mathematics & Statistics. Springer Berlin Heidelberg, pp. 65–75.

Benet, L., Merlo, O., 2008. Multiple Components in Narrow Planetary Rings. Physical Review Letters 100 (1), 014102.

Benet, L., Merlo, O., 2009. Phase-space volume of regions of trapped motion: multiple ring components and arcs. Celestial Mechanics and Dynamical Astronomy 103, 209–225.

Benet, L., Seligman, T. H., 2000. Generic occurrence of rings in rotating systems. Physics Letters A 273, 331–337.

Beurle, K., Murray, C. D., Williams, G. A., Evans, M. W., Cooper, N. J., Agnor, C. B., 2010. Direct evidence for gravitational instability and moonlet formation in saturn's rings. The Astrophysical Journal Letters 718, L176.

Bosh, A. S., Olkin, C. B., French, R. G., Nicholson, P. D., 2002. Saturn's F Ring: Kinematics and Particle Sizes from Stellar Occultation Studies. Icarus 157, 57–75.

Canup, R. M., Esposito, L. W., 1995. Accretion in the Roche zone: Coexistence of rings and ring moons. Icarus 113, 331–352.

Charnoz, S., Dones, L., Esposito, L. W., Estrada, P. R., Hedman, M. M., 2009. Origin and Evolution of Saturn's Ring System. In: Dougherty, M. K., Esposito, L. W., Krimigis, S. M. (Eds.), Saturn from Cassini-Huygens. Springer Netherlands, Ch. 17, pp. 537–575.

Charnoz, S., Porco, C. C., Déau, E., Brahic, A., Spitale, J. N., Bacques, G., Baillie, K., 2005. Cassini Discovers a Kinematic Spiral Ring Around Saturn. Science 310, 1300–1304.

Colwell, J. E., Nicholson, P. D., Tiscareno, M. S., Murray, C. D., French, R. G., Marouf, E. A., 2009. The Structure of Saturn's Rings. In: Dougherty, M. K., Esposito, L. W., Krimigis, S. M. (Eds.), Saturn from Cassini-Huygens. Springer Netherlands, Ch. 13, pp. 375–412.

Cooper, N. J., Murray, C. D., Williams, G. A., 2013. Local Variability in the Orbit of Saturn's F Ring. AJ 145, 161.

Cuzzi, J. N., Burns, J. A., 1988. Charged particle depletion surrounding Saturn's F ring - Evidence for a moonlet belt? Icarus 74, 284–324.

Cuzzi, J. N., Whizin, A. D., Hogan, R. C., Dobrovolskis, A. R., Dones, L., Showalter, M. R., Colwell, J. E., Scargle, J. D., 2014. Saturn's F Ring core: Calm in the midst of chaos. Icarus 232, 157–175.

de la Llave, R., 2001. A tutorial on KAM theory. In: Smooth ergodic theory and its applications (Seattle, WA, 1999). Vol. 69 of Proc. Sympos. Pure Math. Amer. Math. Soc., Providence, RI, pp. 175–292.

El Moutamid, M., Sicardy, B., Renner, S., 2014. Coupling between corotation and Lindblad resonances in the presence of secular precession rates. Celestial Mechanics and Dynamical Astronomy 118, 235–252.

Esposito, L. W., 2006. Planetary Rings. Cambridge University Press, UK.

French, R. G., McGhee, C. A., Dones, L., Lissauer, J. J., 2003. Saturn's wayward shepherds: the peregrinations of Prometheus and Pandora. Icarus 162, 143–170.

French, R. S., Showalter, M. R., Sfair, R., Argüelles, C. A., Pajuelo, M., Becerra, P., Hedman, M. M., Nicholson, P. D., 2012. The brightening of Saturn's F ring. Icarus 219, 181–193.

Gehrels, T., Baker, L. R., Beshore, E., Blenman, C., Burke, J. J., Castillo, N. D., Dacosta, B., Degewij, J., Doose, L. R., Fountain, J. W., Gotobed, J., Kenknight, C. E., Kingston, R., McLaughlin, G., McMillan, R., Murphy, R., Smith, P. H., Stoll, C. P., Strickland, R. N., Tomasko, M. G., Wijesinghe, M. P., Coffeen, D. L., Esposito, L. W., 1980. Imaging photopolarimeter on Pioneer Saturn. Science 207, 434–439.

Giuliatti Winter, S. M., Mourão, D. C., Freitas, T. C. A., 2006. The strands of the F ring disturbed by its closest satellites. Advances in Space Research 38, 781–787.

Giuliatti Winter, S. M., Murray, C. D., Gordon, M., 2000. Perturbations to Saturn's F-ring strands at their closest approach to Prometheus. Planet. Space Sci. 48, 817–827.

Goldreich, P., Rappaport, N., 2003a. Chaotic motions of prometheus and pandora. Icarus 162, 391–399.

Goldreich, P., Rappaport, N., 2003b. Origin of chaos in the Prometheus-Pandora system. Icarus 166, 320–327.

Goldreich, P., Tremaine, S., 1979. Towards a theory for the Uranian rings. Nature 277, 97–99.

Gómez, G., Mondelo, J.-M., Simó, C., 2010. A collocation method for the numerical Fourier analysis of quasi-periodic functions. I. Numerical tests and examples. Discrete Contin. Dyn. Syst. Ser. B 14 (1), 41–74.

Jacobson, R. A., Antreasian, P. G., Bordi, J. J., Criddle, K. E., Ionasescu, R., Jones, J. B., Mackenzie, R. A., Meek, M. C., Parcher, D., Pelletier, F. J., Owen, Jr., W. M., Roth, D. C., Roundhill, I. M., Stauch, J. R., 2006. The Gravity Field of the Saturnian System from Satellite Observations and Spacecraft Tracking Data. AJ 132, 2520–2526.

Jorba, À., Zou, M., 2005. A software package for the numerical integration of ODEs by means of high-order Taylor methods. Experiment. Math. 14 (1), 99–117.

Laskar, J., 1990. The chaotic motion of the solar system - A numerical estimate of the size of the chaotic zones. Icarus 88, 266–291.

Lissauer, J. J., Cuzzi, J. N., 1982. Resonances in saturn's rings. Astronomical Journal 87, 1051.

Luque, A., Villanueva, J., 2014. Quasi-periodic frequency analysis using averaging-extrapolation methods. SIAM J. Appl. Dyn. Syst. 13 (1), 1–46.

Merlo, O., Benet, L., 2007. Strands and braids in narrow planetary rings: a scattering system approach. Celestial Mechanics and Dynamical Astronomy 97, 49–72.

Morbidelli, A., 2002. Modern celestial mechanics : aspects of solar system dynamics. Taylor & Francis, London.

Murray, C. D., Beurle, K., Cooper, N. J., Evans, M. W., Williams, G. A., Charnoz, S., 2008. The determination of the structure of Saturn's F ring by nearby moonlets. Nature 453, 739–744.

Murray, C. D., Chavez, C., Beurle, K., Cooper, N., Evans, M. W., Burns, J. A., Porco, C. C., 2005. How Prometheus creates structure in Saturn's F ring. Nature 437, 1326–1329.

Murray, C. D., Dermott, S. F., 2000. Solar System Dynamics. Cambridge University Press.

Nicholson, P. D., Porco, C. C., 1988. A new constraint on saturn's zonal gravity harmonics from voyager observations of an eccentric ringlet. Journal of Geophysical Research (ISSN 0148-0227) 93, 10209.

Ohtsuki, K., 1993. Capture probability of colliding planetesimals - Dynamical constraints on accretion of planets, satellites, and ring particles. Icarus 106, 228.

Porco, C. C., Baker, E., Barbara, J., Beurle, K., Brahic, A., Burns, J. A., Charnoz, S., Cooper, N., Dawson, D. D., Del Genio, A. D., Denk, T., Dones, L., Dyudina, U., Evans, M. W., Giese, B., Grazier, K., Helfenstein, P., Ingersoll, A. P., Jacobson, R. A., Johnson, T. V., McEwen, A., Murray, C. D., Neukum, G., Owen, W. M., Perry, J., Roatsch, T., Spitale, J., Squyres, S., Thomas, P., Tiscareno, M., Turtle, E., Vasavada, A. R., Veverka, J., Wagner, R., West, R., 2005. Cassini Imaging Science: Initial Results on Saturn's Rings and Small Satellites. Science 307, 1226–1236.

Poulet, F., Sicardy, B., 2001. Dynamical evolution of the Prometheus-Pandora system. MNRAS 322, 343–355.

Poulet, F., Sicardy, B., Nicholson, P. D., Karkoschka, E., Caldwell, J., 2000. Saturn's Ring-Plane Crossings of August and November 1995: A Model for the New F-Ring Objects. Icarus 144, 135–148.

Renner, S., Sicardy, B., 2006. Use of the Geometric Elements in Numerical Simulations. Celestial Mechanics and Dynamical Astronomy 94, 237–248.

Seidelmann, P. K., Archinal, B. A., A'Hearn, M. F., Conrad, A., Consolmagno, G. J., Hestroffer, D., Hilton, J. L., Krasinsky, G. A., Neumann, G., Oberst, J., Stooke, P., Tedesco, E. F., Tholen, D. J., Thomas, P. C., Williams, I. P., 2007. Report of the IAU/IAG Working Group on cartographic coordinates and rotational elements: 2006. Celestial Mechanics and Dynamical Astronomy 98, 155–180.

Showalter, M. R., Burns, J. A., 1982. A numerical study of Saturn's F-ring. Icarus 52, 526–544.

Smith, B. A., Soderblom, L., Batson, R. M., Bridges, P. M., Inge, J. L., Masursky, H., Shoemaker, E., Beebe, R. F., Boyce, J., Briggs, G., Bunker, A., Collins, S. A., Hansen, C., Johnson, T. V., Mitchell, J. L., Terrile, R. J., Cook, A. F., Cuzzi, J. N., Pollack, J. B., Danielson, G. E., Ingersoll, A. P., Davies, M. E., Hunt, G. E., Morrison, D., Owen, T., Sagan, C., Veverka, J., Strom, R., Suomi, V. E., 1982. A new look at the Saturn system - The Voyager 2 images. Science 215, 504–537.

Smith, B. A., Soderblom, L., Beebe, R. F., Boyce, J. M., Briggs, G., Bunker, A., Collins, S. A., Hansen, C., Johnson, T. V., Mitchell, J. L., Terrile, R. J., Carr, M. H., Cook, A. F., Cuzzi, J. N., Pollack, J. B., Danielson, G. E., Ingersoll, A. P., Davies, M. E., Hunt, G. E., Masursky, H., Shoemaker, E. M., Morrison, D., Owen, T., Sagan, C., Veverka, J., Strom, R., Suomi, V. E., 1981. Encounter with Saturn - Voyager 1 imaging science results. Science 212, 163–191.

Tiscareno, M. S., 2013. Planetary Rings. Springer Netherlands, Ch. 7, p. 309.

Winter, O. C., Mourão, D. C., Giuliatti Winter, S. M., Spahn, F., da Cruz, C., 2007. Moonlets wandering on a leash-ring. MNRAS 380, L54–L57.